


Coexisting hinge and vertical disclination states in a higher-order acoustic Dirac semimetal

Yuxin Zhang, Chao Liu, Xiaoyu Dai, and Yuanjiang Xiang^{✉*}
School of Physics and Electronics, Hunan University, Changsha 410082, China

 (Received 13 February 2023; revised 7 May 2023; accepted 14 June 2023; published 23 June 2023)

The concept of crystalline disclinations in solid-state physics has gained attention in recent years, particularly with a focus on two-dimensional C_n -symmetric topological crystalline insulators. Research in this area has revealed novel topological phases different from the traditional bulk-boundary correspondence, expanding the topological material family. However, there remains a need to investigate the bulk-disclination correspondence in three-dimensional topological semimetals. We present an example of a higher-order Dirac semimetal in acoustic crystals with central disclinations. Our simple model not only exhibits hinge modes in the vertical direction but also supports a robust one-dimensional disclination hinge state along the central bulk-hollow path. Simulations demonstrate that our structure is capable of realizing backscatter-free disclination and higher-order hinge waves under the same architecture. Our findings offer insight for potential applications in acoustic devices for sound wave propagation and manipulation, as well as for exploring more exotic high-performance three-dimensional acoustic metamaterials.

DOI: [10.1103/PhysRevB.107.214108](https://doi.org/10.1103/PhysRevB.107.214108)

I. INTRODUCTION

The thriving of band theory in condensed matters physics has promoted the emergence of topological insulators (TIs). One of the remarkable features in TIs is the bulk-edge correspondence principle, where nontrivial boundary states persist in the band gap of the topological materials [1–3]. A system cannot be transferred from a normal insulator (NI) to a TI with small perturbations or disturbances unless the band gap undergoes a closing and reopening process [4–6]. Usually, the n -dimensional (n D) topological material possesses $(n - 1)$ D gapless states at the geometric boundaries or at the interface with NIs. A pool of discoveries such as Chern insulators and quantum spin Hall effects have been proposed and experimentally realized to enrich the topological family [6–8]. Further, the idea of higher-order topological insulators (HOTIs) in recent years has broadened the perspective for studying intriguing nontrivial phases at lower dimensions [9–15]. A HOTI can support $(n - d)$ D lower-dimensional topological states ($d > 1$). It is highlighted that symmetry plays an important role in constituting higher-order phases. Studies reveal that the topological crystalline insulator (TCI) serves as a qualified candidate for a higher-order quadrupole insulator with higher bulk multipole moments [16–20]. In a two-dimensional (2D) TCI the C_n -rotational symmetry makes it endowed with protected corner modes with a fractionalized charge of e/n at each corner [21–27]. In this way, the 2D TCI is naturally transplanted in a three-dimensional (3D) framework following a stacking-layered configuration, and the higher-order topological corner modes become vertical hinge states [28–34].

In parallel, more concepts from condensed matter physics are used to explore novel topological phases, among which lattice defects come into the spotlight due to their unique properties. It is natural to find defects in lattices, and these noneliminated perturbations can also lead to unique physical phenomena despite the local transformation of the real-space structure [35–50]. For example, a screw dislocation in the bulk of a three-dimensional (3D) TI will produce a one-dimensional (1D) helical defect state [48]. Some structures with bulk defects are experimentally demonstrated, such as the 3D acoustic Weyl metamaterials with locked orbital angular momentum [47], 2D photonic TCIs with disclinations [39,45], and light-trapping TIs with dislocations [40]. Among a pool of defects, disclinations built by a “cutting and glue” operation in TIs manifest rich topological properties. Further, disclinations in a simple C_n -symmetric TCI make the design and fabrication of photonic and phononic metamaterials easier and more accessible.

Due to the adequate research on HOTIs, these findings are also spurring the development of topological semimetals (TSMs). A 3D TSM is featured with 2D nonclosed surface arc boundary states, such as the surface Fermi arcs connecting the two Weyl points with opposite charges [51–56]. When it comes to a higher-order topological semimetal (HOTSM), hinge arcs linked by topological charges can be obtained [28–34]. Many of the existing HOTSMs are fabricated with simple C_n -symmetric structures, so it is valuable to investigate the combination of the HOTI and the disclination in a 3D framework.

In this paper, we propose an acoustic higher-order Dirac semimetal (HODSM) with bulk defects that simultaneously manifest the vertical 1D disclination and hinge modes. The model exhibits a C_{6z} symmetry with two Dirac degeneracies along the high-symmetry axis. The topological index describes the higher-order topological phase. At the same

*xiangyuanjiang@126.com

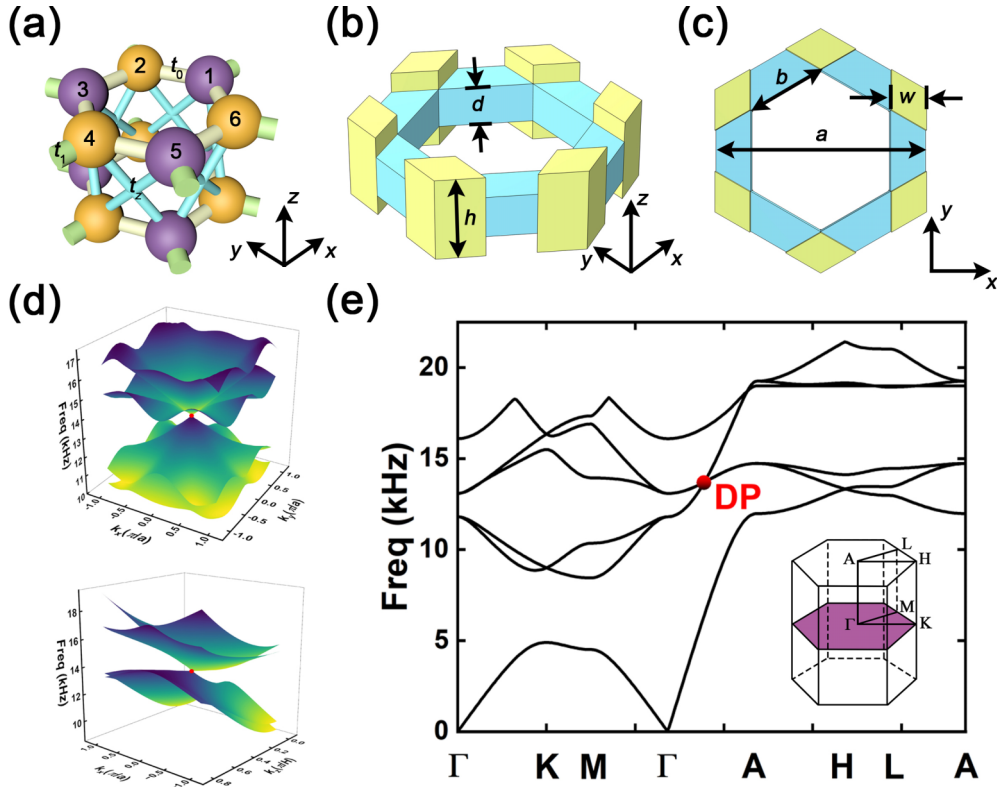


FIG. 1. The framework of our unit cell and corresponding band structure. (a) The tight-binding model of our acoustic lattice. Three connecting bars with different colors stand for intracell (t_0), intercell (t_1), and interlayer (t_z) hopping terms. The unit cell preserves C_{6z} symmetry. (b,c) Constructions of our acoustic crystal. The lattice constants are a and h . (d) Upper panel: The band dispersion near the DP in the k_x-k_y plane. Lower panel: The band crossing mode around the degeneracy point in the k_x-k_z plane. (e) Band structure along the path $\Gamma-K-M-\Gamma-A-H-L-A$, where the fourfold DP is located at the high-symmetry axis $\Gamma-A$. Inset view: the 3D first Brillouin zone of our 3D crystal.

time, the central hollow defects constructed by breaking the lattice configuration lead to the propagation of 1D disclination state along the bulk-hollow path. It is emphasized that the disclination state is explained by the localized inner bound state [45,47], which is different from the hinge modes judged by band topology indicators. We offer a detailed numerical simulation in a multilayer 3D acoustic sample to realize the highly robust hinge and disclination wave transmission and spectral intensity distributions. Our model has successfully illustrated the fascinating one-way confined sound waves protected by two distinct channels, which provides a broader vision for fabricating high-performance acoustic devices such as multimode waveguides under simple piling C_n -symmetric constructions.

II. MODEL CONSTRUCTION AND INVARIANT INDEX MEASUREMENT

We first introduce a minimal acoustic Dirac unit cell in approximation with the tight-binding model, as shown in Fig. 1(a). The overall view of the real acoustic lattice is given in Figs. 1(b) and 1(c) with the horizontal and vertical lattice constants a and h . The lattice supports a higher-order topological phase by adjusting the ratio of intracell and intercell hopping as the k_z passes through the momentum space. We define the in-plane parameters t_0 and t_1 as the intracell and

intercell couplings, respectively. In particular, the interlayer hopping term t_z acts on the in-plane t_0 and makes each monolayer a TCI phase or a NI phase as the k_z varies from $-\pi/h$ to π/h , enabling phase transitions that support a HOTSMS. We can then write the k_z -dependent intracell hopping term as $t_0(k_z) = t_0 + 2t_z \cos(hk_z)$. The thickness of the rigid plate (blue) is d , and the hexagonal pillars' (yellow) width at the six corners is w . This design allows for free transmission of sonic waves to the adjacent unit cell and the neighboring upper or lower lattice, which matches well with the tight-binding model. If we neglect the next nearest neighboring effect, we can model our 3D unit cell with the Hamiltonian matrix as

$$H(\mathbf{k}) = \begin{bmatrix} 0 & A & 0 & B^\dagger & 0 & A \\ A & 0 & A & 0 & C^\dagger & 0 \\ 0 & A & 0 & A & 0 & D^\dagger \\ B & 0 & A & 0 & A & 0 \\ 0 & C & 0 & A & 0 & A \\ A & 0 & D & 0 & A & 0 \end{bmatrix}, \quad (1)$$

where $A = t_0 + 2t_z \cos(hk_z)$, $B = t_1 e^{ik_x a}$, $C = t_1 e^{i(k_x/2 + k_y \sqrt{3}/2)a}$, and $D = t_1 e^{-i(k_x/2 - k_y \sqrt{3}/2)a}$.

We choose the setting of $t_0 = t_1 = -1$ and $t_z = -1/4$ and find the Dirac points (DPs) at $k = (0, 0, 0.4\pi/h)$ along the $\Gamma-A$ axis. According to the C_{6z} symmetry, the DP will also appear at $k = (0, 0, -0.4\pi/h)$. Figure 1(d) shows the band

dispersion modes in three directions, where the band crossing modes around the DP indicate that our HODSM is a type-II semimetal. To agree with the theoretical results, we use the finite-size analysis to calculate the band structure of the unit cell along the 3D first Brillouin zone (FBZ) in Fig. 1(e). This way, we fit the sample parameters of $a = 27.7$ mm, $h = 9.6$ mm, $d = 4.8$ mm, $w = 4.6$ mm, and $b = 10$ mm to obtain the simulation band spectrum. As can be seen in the band structure, the type-II DP appears at $k = (0, 0, 0.4\pi/h)$ with a frequency of around 13.7 kHz, proving that our model can be well interpreted with a tight-binding approximation.

Since our lattice observes C_{6z} rotational-mirror symmetry, we can characterize the topological phases at each k_z by the invariant index $\chi^{(6)} = ([M_1^{(2)}], [K_1^{(3)}])$ [19,35,38–40]. The $[M_1^{(2)}]$ and $[K_1^{(3)}]$ denote the different band representations of the occupied energy bands at the high-symmetry momentum points Γ , K , and M . The C_2 invariants is defined as $[M_1^{(2)}] = \#M_1^{(2)} - \#\Gamma_1^{(2)}$, where M is the twofold high-symmetry momentum invariant point under the C_2 rotational operator. Similarly, the C_3 invariants can be expressed as $[K_1^{(3)}] = \#K_1^{(3)} - \#\Gamma_1^{(3)}$, where K is the threefold rotational invariant points in the momentum space [57,58]. $\#M_1^{(2)}$ ($\#K_1^{(3)}$) and $\#\Gamma_1^{(2)}$ ($\#\Gamma_1^{(3)}$) are the numbers of energy bands under band gaps with C_2 (C_3) rotational eigenvalues of +1 at high-symmetry momentum points M (K) and Γ . As k_z crosses the FBZ, the k_z -dependent ratio of $t_1/t_0(k_z)$ changes, describing the phase transition process by judging the changing $\chi^{(6)}$ (see Supplemental Material [59]). Therefore, we can calculate the band structure at $k_z = 0.3\pi/h$ and $0.8\pi/h$ to verify the $\chi^{(6)}$ in two different topological phases, as shown in Figs. 2(a) and 2(b). At each high-symmetry momentum point below the band gap, we label the C_n point groups with irreducible representations and corresponding phase winding profiles in Figs. 2(d) and 2(e). In Fig. 2(c), we find that when $0 < k_z < 0.4\pi/h$, $[M_1^{(2)}]$ and $[K_1^{(3)}]$ remain zero, indicating a NI phase, while $\chi^{(6)} = (-2, 0)$ when $0.4\pi/h < |k_z| < \pi/h$, indicating a nontrivial TCI phase. Figure 2(f) shows the phase transition diagram of our k_z -dependent monolayer unit cell, where the two DPs represent the phase transition points at $k_z = 0.4\pi/h$. For a TCI phase, the Wannier centers are on the sides of the lattice and the corner charge hosts. On the other hand, the Wannier centers are concentrated on the middle of the crystal when the system transforms into a NI phase. The central black circle illustrates the path of the phase transition process, where the closed loop experiences both TCI and NI phases by crossing the interface of the two different areas. The two DPs (red dots) are the case of equal intracell and intercell coupling strength.

III. DISCLINATIONS IN THE 3D HOTI ARCHITECTURE

It is revealed that a 2D C_n -symmetric unit cell can be divided into n sectors like a pizza, and each sector has an angle of $2\pi/n$ from the rotation axis, as plotted in Fig. 3(a). Protected by the C_n symmetry, these sectors are invariant under C_n rotational operations. To introduce a disclination, we can either insert or remove $1/n$ part of the plate lattice, that is, the glue-stick process [45–47]. In this way, a zero-dimensional (0D) disclination mode will emerge in the trapped central

defect. In our framework, a Frank angle $\Omega = 2\pi/6$ sector of the plane is cut and glued to constitute a deformed disclination metacell structure, as displayed in Fig. 3(b) [39,45–47]. As analyzed before, the sample possesses a fractional corner charge as long as the system stays in a TCI phase, since the loss of one sector will not destroy the rotational invariant property of the remaining $(n - 1)$ parts. For a NI phase, the meta-array will not manifest corner modes at the five corners, while the TCI phase hosts corner states, and the Wannier centers in the TCI contribute to a fractional corner charge of $e/2$ [21,45,46]. Figure 3(c) gives the band projection spectrum of the disclination-introduced metacell, where a “disclination hinge” (marked by hollow green circles) spans the k_z axis and merges into the bulk bands around $k_z = 0.75\pi/h$. Generally speaking, the localized disclination states can survive in the continuum spectrum and hybridize with bulk states and become indistinguishable. In a regular C_{6z} -symmetric metacell, only hinge arcs connected by the two DPs will emerge between the bulk bands in the range $0.4\pi/h < |k_z| < \pi/h$. After introducing the disclination, the deformed finite-size sample will inherit the fractional corner charge protected by the higher-order invariant index among $0.4\pi/h < |k_z| < \pi/h$. When k_z travels in the TCI phase, the Wannier centers are located at the boundary of the unit cell as shown in Fig. 2(a); thus each sector of the metaplane will contribute an $e/2$ fractional charge, as displayed at Fig. 3(b). So the disclination state also has the $e/2$ fractional charge. When k_z locates in the NI phase, the Wannier centers all gather in the middle of the unit cell; the disclination core hosts no fractional charge. However, the central core is a vertical path with air transmission along the k_z direction in the momentum space. The bound state around the disclination for each k_z is regarded as the 2D bound modes triggered by localized defects, since the disclination itself originated from the bulks [47]. Therefore, this inner sonic wave propagation will not be affected by the changing intracell hopping as the k_z goes. Also, the disclination arc connects the two symmetry-pinned DPs at $k_z = \pm 0.4\pi/h$, as described in Fig. 3(c). Distinguished from other approaches such as screw-glide disclination defects in 3D crystals, our framework can be achieved without too many geometrical distortions, which is vital for practical fabrication. More importantly, we can make other deformed metacells by inserting the $1/n$ part of the C_n -symmetric plane to build central-filled disclination modes. For example, the C_3 - or C_4 -symmetric TCIs can be expanded into a defected finite-size sample preserving C_4 or C_5 rotational symmetry.

Further, we investigate the eigenstate solutions of different phases to see acoustic field distributions. In Fig. 4(a), we choose $k_z = 0.2\pi/h$ of the unit cell in NI phases and corresponding eigenstate modes. We have marked the Wannier center locations in each unit cell (red dots), where the corner charge will not appear due to the principle of fractional charge distribution in the NI phase, while for $k_z = 0.6\pi/h$, both the hinge and disclination modes exist since the Wannier center is sitting on the sides of each unit cell (yellow dots), as shown in Fig. 4(b). The hinge charge at each corner is $Q_c = \{e/4[M_1^{(2)}] + e/6[K_1^{(3)}]\} \bmod e$, where $Q_c = 0$ in a NI phase and $Q_c = e/2$ in the TCI phase [45–47]. The inset views of Figs. 4(a) and 4(b) show the acoustic pressure field distribution of the disclination mode at $k_z = 0.2\pi/h$ and $0.6\pi/h$.

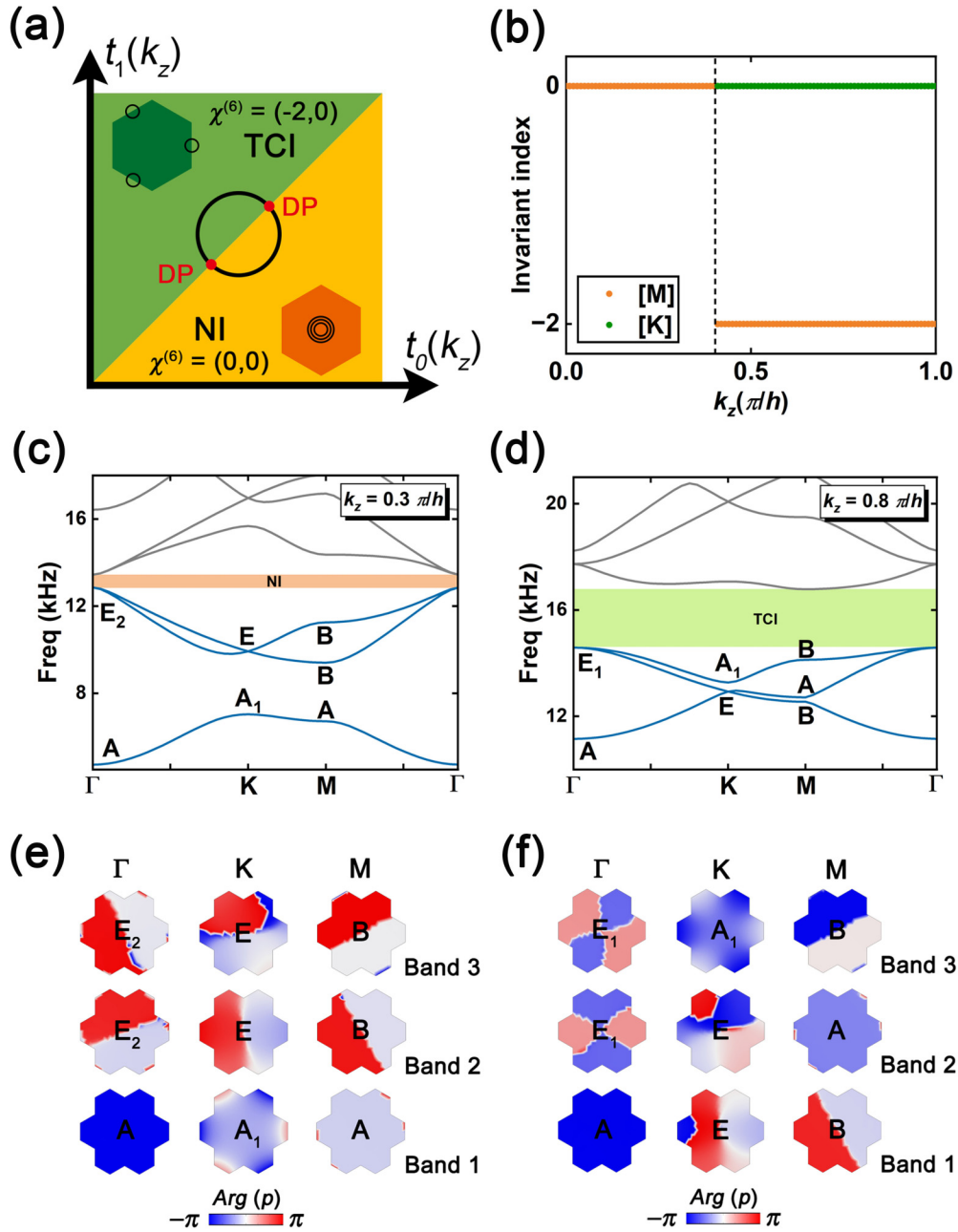


FIG. 2. The invariant index and band structures as k_z varies. (a,b) The band spectra of Γ - K - M - Γ at $k_z = 0.3\pi/h$ and $0.8\pi/h$. The irreducible representations of C_n -rotational eigenvalues at high-symmetry momentum points are given. (c) The calculation results of $[M_1^{(2)}]$ and $[K_1^{(3)}]$ with the range of $0 < k_z < \pi/h$. The phase transition point at $k_z = 0.4\pi/h$ divides the system into HOTI and NI phases. (d,f) The phase winding properties of high-symmetry momentum points at lower bands. (f) Topological phase diagram of our HODSM with a k_z -dependent coupling ratio. The Wannier centers are marked for TCI and NI phases. The black loop describes the topology properties of the system as k_z changes. DPs are pinned at the interface of the TCI and NI regions.

The fivefold rotational symmetry protected defect-introduced metalattice plate owns a disclination charge of

$$Q_d = e \{ \Omega / 2\pi (3/2 [M_1^{(2)}] - [K_1^{(3)}]) \} \bmod e = e/2 \quad (2)$$

in the TCI phase [45–47]. Additionally, the disclination charge is zero in the NI phase. From the eigenmode solutions in Fig. 4(b), we find that the numbers of hinge and disclination states are five and one. There are five defect modes due to the mirror symmetry in a fivefold TCI sample, including two pairs of symmetric and antisymmetric disclination states and a

single mode. The remaining four disclination modes are mixed with the bulk states and fail to be unambiguously confirmed.

IV. ROBUSTNESS OF THE DISCLINATION STATE TRANSMISSION

We perform the finite-element method to simulate the acoustic pressure field distribution in approximation with real-space near-field measurement. To this end, we construct a

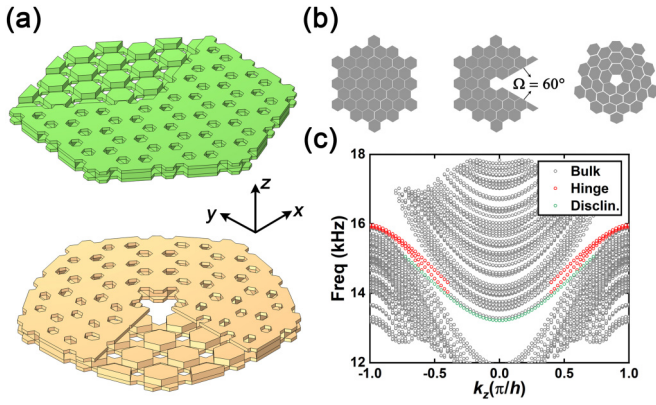


FIG. 3. Design of our 3D acoustic HODSM metaplane and disclination sample. (a) Upper panel: The monolayer finite-size sample composed of HODSM crystals, where the green part stands for the air region. The top layer is partly removed to show the inside air cavities. Lower panel: The deformed HODSM sample with central bulk defects, where the orange part is the air region. (b) The formulation procedure of a disclination metacell. By removing a $\pi/3$ part of the plane sample and reattaching the two edges by deforming the remaining lattices, the bulk defects generate in the middle of the metacrystal. (c) The hinge and disclination projection spectrum of the defect-introduced finite-size sample.

13-layer metacell sample with disclinations in the central part of the structure, as shown in Fig. 5(a). The gray, green, and purple solid circles are probes inserted into the multilayer acoustic metamaterials. One-fifth of the architecture is removed to better display the inner structure. The five side boundary surfaces of the piling sample and the central disclination tunnel are set as rigid hard boundary conditions to block the air transmission. Figure 5(b) gives the calculated bulk, hinge, and disclination mode transmission rate, where the hinge and disclination states reach peak values of around 15.75 kHz. Due to the merging of topological and bulk bands,

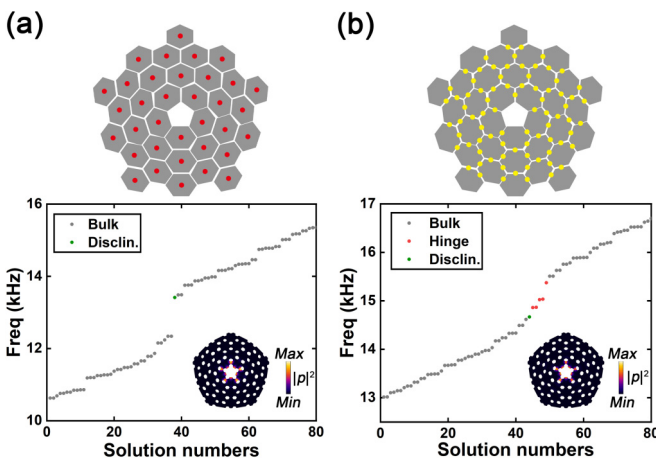


FIG. 4. The eigensolutions of finite-size acoustic HODSM in TCI and NI phases. (a,b) Upper plane: the spectral charges of the unit cells in a whole structure at $k_z = 0.3\pi/h$ and $0.7\pi/h$. Lower plane: The eigenmodes spectrum at $k_z = 0.2\pi/h$ and $0.6\pi/h$, where gray dots mean bulk modes, green dots represent disclination modes, and red dots denote hinge modes. The inset view plots the acoustic pressure $|p|^2$ distribution near the bulk defects.

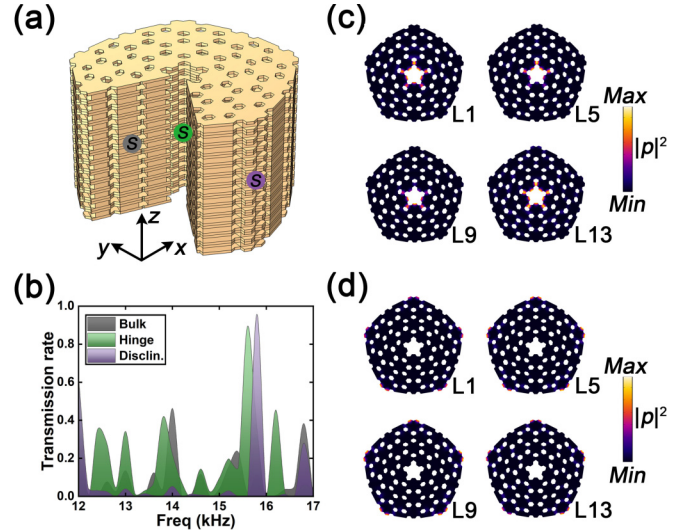


FIG. 5. Constructions of the multilayer acoustic HODSM sample with disclinations. (a) The 3D view of our stacking metacell (only air regions are shown), where the acoustic probes are placed in the middle of the sample to detect bulk, hinge, and disclination modes. (b) The transmission rate spectrum of our sample with hinge (green), disclination (purple), and bulk (gray) modes. The hinge and disclination states reach peak values at a frequency around 15.75 kHz. (c) Acoustic field distributions of disclination states at layers 1, 5, 9, and 13 at 14.9 kHz. (d) Acoustic field distributions of hinge states at layers 1, 5, 9, and 13 at 15.1 kHz.

we find a spectrum mixture at 13–15 kHz frequency. To study the sonic wave propagation performance, we put the excitation sources near the hinge and the central disclination at the top of the sample to simulate the robust one-way transmission. We extract different layers of acoustic field slices, as displayed in Figs. 5(c) and 5(d). Disclination and hinge modes are firmly pinned at layers 1 (L1), 5 (L5), 9 (L9), and 13 (L13) (counting from the top layer) at frequencies of 14.9 and 15.1 kHz, indicating a well-performed vertical wave propagation in confined directions.

Then we pay attention to the robustness of our bulk-disclination acoustic HODSM against system disorders. Two main defects must be considered: (i) broken rotation symmetry and (ii) irregular disclination shape. In Figs. 6(b) and 6(d), we erase one unit cell near the central hollow space; hence, both the rotational symmetry and disclination shape will be disrupted. Again, we select the NI and TCI phases to examine the eigenmode solutions with disorders. In Fig. 6(a), we obtain the solution numbers of the disorder-induced disclination plane at $k_z = 0.2\pi/h$. The strongly localized disclination modes can be seen around the defects and extended disorders in the center of the sample. Figure 6(a) plots five disclination states among the bulk band gap due to the broken mirror symmetry. In particular, Fig. 6(c) shows that in the TCI phase a disorder will produce a mixture state containing both hinge and disclination modes. The acoustic field distribution of sample slices in Fig. 6(d) explicitly presents mixture states at 14.61 and 14.94 kHz, and the solutions manifest a hinge mixture disclination hierarchy in the band gap. The emergence of mixture states is attributed to the inner hinge shape, where the

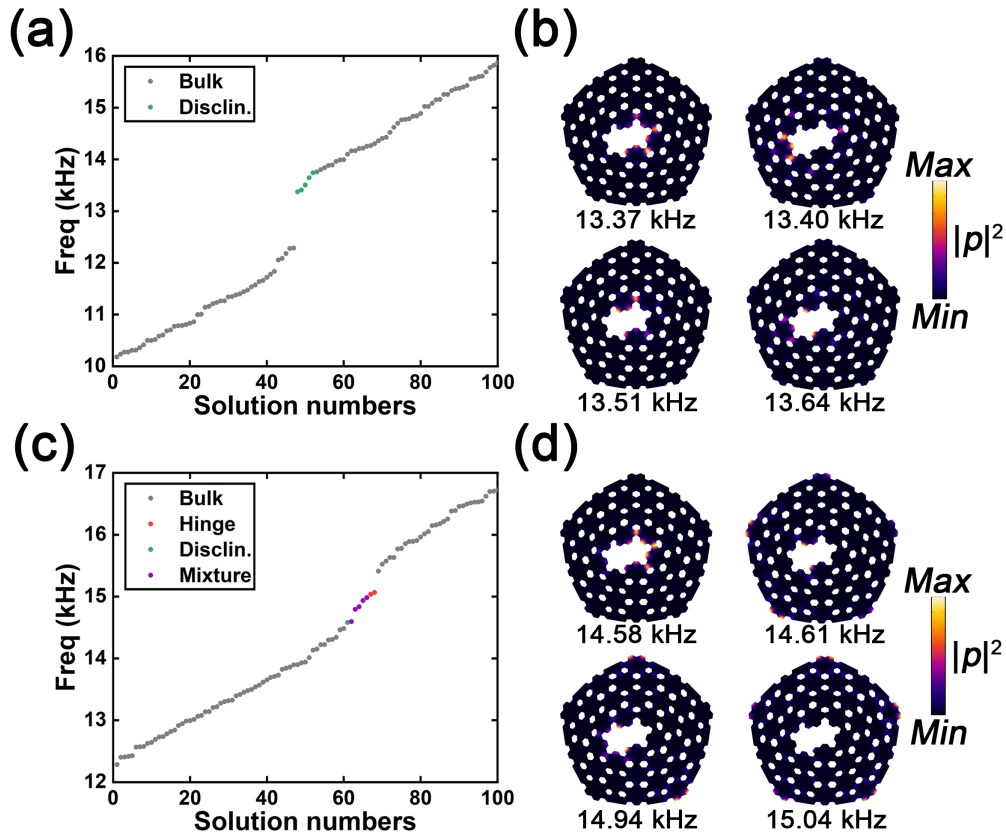


FIG. 6. Simulations on acoustic metacell sample with bulk defects and disorders and corresponding field distributions. (a) Eigenmode solutions of the disturbed lattice in the NI phase at $k_z = 0.2\pi/h$. (b) Acoustic pressure field intensity of disclination states in a NI phase at 13.37, 13.40, 13.51, and 13.64 kHz. (c) Eigenmode solutions of the disturbed lattice in the TCI phase at $k_z = 0.6\pi/h$. (d) Acoustic pressure field intensity of disclination and mixture states in the TCI phase at 14.58, 14.61, 14.94, and 15.04 kHz.

initial bulk defect and added disorders constitute the acoustic field concentration.

V. CONCLUSIONS

In conclusion, we have proposed a higher-order acoustic HODSM with vertical disclinations. Apart from the higher-order hinge states in a piling 3D structure, central-localized disclination states also emerge. The cutting and glue operation creates a central disclination derived from the bulk, where the boundary state separates from the continuum bulk spectrum. We use band topology theory to analyze the invariant index at a varying k_z to measure the NI and TCI phases. The projected band spectrum on our defect-introduced HODSM plate shows the relative pure disclination arc throughout the momentum space accompanying with higher-order hinge modes.

Simulations prove a well-performed sonic wave propagation along the hinge and disclination path. Also, the localized disclination modes are robust against system disorders by breaking the mirror and rotational symmetry. Our proposal provides an approach to designing and fabricating a high-performance acoustic device to realize high-efficiency waveguides and to modeling the flow of sonic waves in tube cavity shaped metamaterials.

ACKNOWLEDGMENTS

This work is partially supported by the National Natural Science Foundation of China (Grants No. 61875133 and No. 11874269), the Natural Science Foundation of Hunan Province (Grants No. 2021JJ30135 and No. 2021JJ30149), and the Chongqing Natural Science Foundation (Grant No. CSTB2022NSCQ-MSX0872).

- [1] K. V. Klitzing, G. Dorda, and M. Pepper, New Method for High-Accuracy Determination of the Fine-Structure Constant Based on Quantized Hall Resistance, *Phys. Rev. Lett.* **45**, 494 (1980).
- [2] M. Z. Hasan and C. L. Kane, Colloquium: Topological insulators, *Rev. Mod. Phys.* **82**, 3045 (2010).
- [3] A. Bansil, H. Lin, and T. Das, *Colloquium: Topological band theory*, *Rev. Mod. Phys.* **88**, 021004 (2016).

- [4] A. A. Soluyanov and D. Vanderbilt, Computing topological invariants without inversion symmetry, *Phys. Rev. B* **83**, 235401 (2011).
- [5] R. Roy, Topological phases and the quantum spin Hall effect in three dimensions, *Phys. Rev. B* **79**, 195322 (2009).
- [6] X.-G. Wen, Colloquium: Zoo of quantum-topological phases of matter, *Rev. Mod. Phys.* **89**, 041004 (2017).

- [7] Y.-J. Ding, Y.-G. Peng, Y.-F. Zhu, X.-D. Fan, J. Yang, B. Liang, X.-F. Zhu, X.-G. Wan, and J.-C. Cheng, Experimental Demonstration of Acoustic Chern Insulators, *Phys. Rev. Lett.* **122**, 014302 (2019).
- [8] B. A. Bernevig and S.-C. Zhang, Quantum Spin Hall Effect, *Phys. Rev. Lett.* **96**, 106802 (2006).
- [9] W. A. Benalcazar, B. A. Bernevig, and T. L. Hughes, Quantized electric multipole insulators, *Science* **357**, 61 (2017).
- [10] Q. Wei, X.-W. Zhang, W.-Y. Deng, J.-Y. Lu, X.-Q. Huang, M. Yan, G. Chen, Z.-Y. Liu, and S.-T. Jia, 3D Hinge Transport in Acoustic Higher-Order Topological Insulators, *Phys. Rev. Lett.* **127**, 255501 (2021).
- [11] Z. Song, Z. Fang, and C. Fang, ($d - 2$) Dimensional Edge States of Rotation Symmetry Protected Topological States, *Phys. Rev. Lett.* **119**, 246402 (2017).
- [12] Y.-T. Yang, J.-Y. Lu, M. Yan, X.-Q. Huang, W.-Y. Deng, and Z.-Y. Liu, Hybrid-Order Topological Insulators in a Phononic Crystal, *Phys. Rev. Lett.* **126**, 156801 (2021).
- [13] B.-Y. Xie, G.-X. Su, H.-F. Wang, H. Su, X.-P. Shen, P. Zhan, M.-H. Lu, Z.-L. Wang, and Y.-F. Chen, Visualization of Higher-Order Topological Insulating Phases in Two-Dimensional Dielectric Photonic Crystals, *Phys. Rev. Lett.* **122**, 233903 (2019).
- [14] Y. Ota, F. Liu, R. Katsumi, K. Watanabe, K. Wakabayashi, Y. Arakawa, and S. Iwamoto, Photonic crystal nanocavity based on a topological corner state, *Optica* **6**, 786 (2019).
- [15] Y.-X. Zhang, Z.-F. Li, S.-X. Xu, and Y.-J. Xiang, Tunable and reconfigurable higher-order topological insulators in photonic crystals with phase change materials, *Ann. Phys. (Berlin)* **534**, 2100293 (2021).
- [16] L. Fu, Topological Crystalline Insulators, *Phys. Rev. Lett.* **106**, 106802 (2011).
- [17] C. Fang and L. Fu, New classes of three-dimensional topological crystalline insulators: Nonsymmorphic and magnetic, *Phys. Rev. B* **91**, 161105(R) (2015).
- [18] J.-W. Liu, W.-H. Duan, and L. Fu, Two types of surface states in topological crystalline insulators, *Phys. Rev. B* **88**, 241303(R) (2013).
- [19] X.-Y. Dong and C.-X. Liu, Classification of topological crystalline insulators based on representation theory, *Phys. Rev. B* **93**, 045429 (2016).
- [20] M. Ezawa, Topological Switch between Second-Order Topological Insulators and Topological Crystalline Insulators, *Phys. Rev. Lett.* **121**, 116801 (2018).
- [21] W. A. Benalcazar, T.-H. Li, and T. L. Hughes, Quantization of fractional corner charge in C_n -symmetric higher-order topological crystalline insulators, *Phys. Rev. B* **99**, 245151 (2019).
- [22] S.-F. Qian, G.-B. Liu, C.-C. Liu, and Y.-G. Yao, C_n -symmetric higher-order topological crystalline insulators in atomically thin transition metal dichalcogenides, *Phys. Rev. B* **105**, 045417 (2022).
- [23] R. Takahashi, T.-T. Zhang, and S. Murakami, General corner charge formula in two-dimensional C_n -symmetric higher-order topological insulators, *Phys. Rev. B* **103**, 205123 (2021).
- [24] C. W. Peterson, T.-H. Li, W. A. Benalcazar, T. L. Hughes, and G. Bahl, A fractional corner anomaly reveals higher-order topology, *Science* **368**, 1114 (2020).
- [25] M. Hirayama, R. Takahashi, S. Matsuishi, H. Hosono, and S. Murakami, Higher-order topological crystalline insulating phase and quantized hinge charge in topological electride apatite, *Phys. Rev. Res.* **2**, 043131 (2020).
- [26] M.-Y. Li, D. Zhirihin, M. Gorbach, X. Ni, D. Filonov, A. Slobozhanyuk, A. Alù, and A. B. Khanikaev, Higher-order topological states in photonic kagome crystals with long-range interactions, *Nat. Photonics* **14**, 89 (2020).
- [27] J.-C. Bao, D.-Y. Zou, W.-X. Zhang, W.-J. He, H.-J. Sun, and X.-D. Zhang, Topoelectrical circuit octupole insulator with topologically protected corner states, *Phys. Rev. B* **100**, 201406(R) (2019).
- [28] M. Lin and T. L. Hughes, Topological quadrupolar semimetals, *Phys. Rev. B* **98**, 241103(R) (2018).
- [29] Z.-H. Wang, D.-J. Liu, H.-T. Teo, Q. Wang, H.-R. Xue, and B.-L. Zhang, Higher-order Dirac semimetal in a photonic crystal, *Phys. Rev. B* **105**, L060101 (2022).
- [30] Y.-X. Zhang, J. Tang, X.-Y. Dai, S. Zhang, Z.-Z. Cao, and Y.-J. Xiang, Design of a higher-order nodal-line semimetal in a spring-shaped acoustic topological crystal, *Phys. Rev. B* **106**, 184101 (2022).
- [31] H.-H. Qiu, M. Xiao, F. Zhang, and C.-Y. Qiu, Higher-Order Dirac Sonic Crystals, *Phys. Rev. Lett.* **127**, 146601 (2021).
- [32] Y.-X. Zhang, J. Tang, X.-Y. Dai, S. Zhang, and Y.-J. Xiang, Higher-order nodal ring photonic semimetal, *Opt. Lett.* **47**, 5885 (2022).
- [33] H.-X. Wang, Z.-K. Lin, B. Jiang, G.-Y. Guo, and J.-H. Jiang, Higher-Order Weyl Semimetals, *Phys. Rev. Lett.* **125**, 146401 (2020).
- [34] Q. Wei, X.-W. Zhang, W.-Y. Deng, J.-Y. Lu, X.-Q. Huang, M. Yan, G. Chen, Z.-Y. Liu, and S.-T. Jia, Higher-order topological semimetal in acoustic crystals, *Nat. Mater.* **20**, 812 (2021).
- [35] Y. Ran, Y. Zhang, and A. Vishwanath, One-dimensional topologically protected modes in topological insulators with lattice dislocations, *Nat. Phys.* **5**, 298 (2009).
- [36] J. Paulose, B. G. Chen, and V. Vitelli, Topological modes bound to dislocations in mechanical metamaterials, *Nat. Phys.* **11**, 153 (2015).
- [37] G. Miert and C. Ortix, Dislocation charges reveal two-dimensional topological crystalline invariants, *Phys. Rev. B* **97**, 201111(R) (2018).
- [38] E. Lustig, L. J. Maczewsky, J. Beck, T. Biesenthal, M. Heinrich, Z.-J. Yang, Y. Plotnik, A. Szameit, and M. Segev, Photonic topological insulator induced by a dislocation in three dimensions, *Nature (London)* **609**, 931 (2022).
- [39] C. W. Peterson, T.-H. Li, W.-T. Jiang, T. L. Hughes, and G. Bahl, Trapped fractional charges at bulk defects in topological insulators, *Nature (London)* **589**, 376 (2021).
- [40] F.-F. Li, H.-X. Wang, Z. Xiong, Q. Lou, P. Chen, R.-X. Wu, Y. Poo, J.-H. Jiang, and S. John, Topological light-trapping on a dislocation, *Nat. Commun.* **9**, 2462 (2018).
- [41] Q. Wang, H.-R. Xue, B.-L. Zhang, and Y. D. Chong, Observation of Protected Photonic Edge States Induced by Real-Space Topological Lattice Defects, *Phys. Rev. Lett.* **124**, 243602 (2020).
- [42] R. J. Slager, A. Mesaros, V. Juričić, and J. Zaanen, The space group classification of topological band-insulators, *Nat. Phys.* **9**, 98 (2013).
- [43] R. J. Slager, A. Mesaros, V. Juričić, and J. Zaanen, Interplay between electronic topology and crystal symmetry: Dislocation-line modes in topological band insulators, *Phys. Rev. B* **90**, 241403(R) (2014).

- [44] V. Juričić, A. Mesaros, R. J. Slager, and J. Zaanen, Universal Probes of Two-Dimensional Topological Insulators: Dislocation and Π Flux, *Phys. Rev. Lett.* **108**, 106403 (2012).
- [45] Y. Liu, S.-W. Leung, F.-F. Li, Z.-K. Lin, X.-F. Tao, Y. Poo, and J.-H. Jiang, Bulk–disclination correspondence in topological crystalline insulators, *Nature (London)* **589**, 381 (2021).
- [46] T.-H. Li, P.-H. Zhu, W. A. Benalcazar, and T. L. Hughes, Fractional disclination charge in two-dimensional C_n -symmetric topological crystalline insulators, *Phys. Rev. B* **101**, 115115 (2020).
- [47] Q. Wang, Y. Ge, H.-X. Sun, H.-R. Xue, D. Jia, Y.-J. Guan, S.-Q. Yuan, B.-L. Zhang, and Y. D. Chong, Vortex states in an acoustic Weyl crystal with a topological lattice defect, *Nat. Commun.* **12**, 3654 (2021).
- [48] L. Ye, C. Qiu, M. Xiao, T. Li, J. Du, M. Ke, and Z. Liu, Topological dislocation modes in three-dimensional acoustic topological insulators, *Nat. Commun.* **13**, 508 (2022).
- [49] H. Hamasaki, Y. Tokumoto, and K. Edagawa, Dislocation conduction in Bi-Sb topological insulators, *Appl. Phys. Lett.* **110**, 092105 (2017).
- [50] Y. Yoshimura, A. Matsumoto, Y. Takane, and K. Imura, Perfectly conducting channel on the dark surface of weak topological insulators, *Phys. Rev. B* **88**, 045408 (2013).
- [51] S. M. Young, S. Zaheer, J. C. Y. Teo, C. L. Kane, E. J. Mele, and A. M. Rappe, Dirac Semimetal in Three Dimensions, *Phys. Rev. Lett.* **108**, 140405 (2012).
- [52] N. P. Armitage, E. J. Mele, and A. Vishwanath, Weyl and Dirac semimetals in three-dimensional solids, *Rev. Mod. Phys.* **90**, 015001 (2018).
- [53] C. Fang, M. J. Gilbert, X. Dai, and B. A. Bernevig, Multi-Weyl Topological Semimetals Stabilized by Point Group Symmetry, *Phys. Rev. Lett.* **108**, 266802 (2012).
- [54] L. Lu, Z.-Y. Wang, D.-X. Ye, L.-X. Ran, L. Fu, J. D. Joannopoulos, and M. Soljačić, Experimental observation of Weyl points, *Science* **349**, 622 (2015).
- [55] X.-G. Wan, A. M. Turner, A. Vishwanath, and S. Y. Savrasov, Topological semimetal and Fermi-arc surface states in the electronic structure of pyrochlore iridates, *Phys. Rev. B* **83**, 205101 (2011).
- [56] F. Li, X.-Q. Huang, J.-Y. Lu, J.-H. Ma, and Z.-L. Liu, Weyl points and Fermi arcs in a chiral phononic crystal, *Nat. Phys.* **14**, 30 (2018).
- [57] J. Kruthoff, J. de Boer, J. van Wezel, C. L. Kane, and R.-J. Slager, Topological Classification of Crystalline Insulators through Band Structure Combinatorics, *Phys. Rev. X* **7**, 041069 (2017).
- [58] Z.-K. Lin and J.-H. Jiang, Dirac cones and higher-order topology in quasi-continuous media, *Europhys. Lett.* **137**, 15001 (2022).
- [59] See Supplemental Material at <http://link.aps.org/supplemental/10.1103/PhysRevB.107.214108> for the topological classification of the acoustic HODSM structure.